Heliyon 8 (2022) e09680

Contents lists available at ScienceDirect

Heliyon

journal homepage: www.cell.com/heliyon

Research article

Effect of process parameters on microstructures and properties of Al–42Si alloy fabricated by selective laser melting

Xiaoye Cai [a], Tong Liu [a,b,*], Xuan Yan [b], Zonghui Cheng [a], Lu Pan [c,**], Zongjun Tian [d], Liangshun Luo [e], Yanqing Su [e]

[a] State-Owned Wuhu Machinery Factory, Wuhu, 241007, PR China
[b] Anhui Key Laboratory of High-performance Non-ferrous Metal Materials, Anhui Polytechnic University, Wuhu, 241000, PR China
[c] Anhui Technical College of Mechanical and Electrical Engineering, Wuhu, 241000, PR China
[d] College of Mechanical and Electrical Engineering, Nanjing University of Aeronautics and Astronautics, Nanjing, 210016, PR China
[e] Anhui HIT3D Additive Technology Co. Ltd., Wuhu, 241200, PR China

ARTICLE INFO

Keywords:
Al-42Si alloy
Selective laser melting
Process parameters
Microstructures

ABSTRACT

In this paper, high-silicon Al–42Si alloy was prepared by selective laser melting (SLM) with different process parameters. Microstructures evolution and defects formation were studied and process parameters were optimized. The results shown that the density of SLM-fabricated Al–42Si alloy increases as input energy density increases. The highest and lowest density of SLM-fabricated Al–42Si alloy are obtained, when input energy density is 42.9J/mm^3 and 33.8J/mm^3 respectively. The microstructures of Al–42Si alloy fabricated by selective laser melting is mainly composed of primary silicon phase and eutectic silicon phase, which is distinct from casting alloy because of diffient grains size and shapes of the primary silicon. With higher energy density, larger size of the primary silicon observed during process due to higher heat released by powder. The size of primary silicon phase particles is in the range of 2.9–9.4μm, and the size of molten pool during SLM process is in the range of 125 ± 10μm–140 ± 10μm in this study. Also the hardness of SLM-fabricated Al–42Si alloy increases as input energy density increases between 40.0J/mm^3 and 42.9J/mm^3. After heat treatment, the residual stress is eliminated, microstructure stability and homogeneous of SLM-fabricated Al–42Si alloy are improved. The silicon distribution is more uniform and sizes increases about 1~2μm, and the hardness decreases after heat treatment. The optimal SLM parameters for Al–42Si alloy are laser power of 320W, scanning speed of 1355 mm/s, layer thickness of 50μm and scanning space of 110μm.

1. Introduction

High silicon aluminum alloy have emerged as new type of electronic material because of high thermophysical properties, low coefficient of thermal expansion and stable chemical properties [1, 2]. High silicon aluminum alloy such as Al–42Si alloy is widely used in aerospace industry and modern electronic information technology and other high-tech fields. High-silicon Al–Si alloy prepared by traditional processing methods such as casting usually exhibit coarse grain sizes and uneven microstructure, this typical microstructures tend to poor mechanical properties of the alloys [3, 4]. Therefore, it is important to improve the mechanical properties of high-silicon Al–Si alloy by grain sizes refinement and microstructure modification.

Selective laser melting (SLM) technology uses a high-energy laser as the heat source, and then melts the metal powder based on the three-dimensional model. The powder melts quickly and solidifies layer by layer to fabricate high-performance, high-precision components with complex geometries, and the components can be used only by simple polishing without complicated processing [5, 6, 7, 8]. SLM has multiple rapid melting and solidification processes, which can increase nucleation sites and refine the structure. SLM has been widely used to fabricate range of materials, including Fe-based alloys [9, 10, 11], Al-based alloys [12, 13], Ni-based alloys and Ti-based alloys [14, 15, 16, 17].

The microstructures produced by SLM are very fine usually and present duplex grain structure. Also SLM technology can increase the

* Corresponding author.
** Corresponding author.
E-mail addresses: liutong@ahpu.edu.cn (T. Liu), ahjdpanlu@126.com (L. Pan).

https://doi.org/10.1016/j.heliyon.2022.e09680
Received 23 January 2022; Received in revised form 12 March 2022; Accepted 1 June 2022

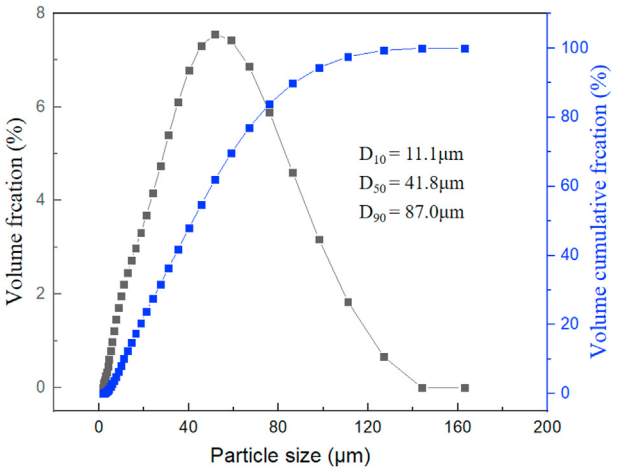

Figure 1. Powder particle size distribution of Ti–42Si alloy.

strength of alloys and shorten the components fabricate cycle, and has broad development prospects in industrial manufacturing [18].

Aluminum alloy powder easily forms an oxide film on the surface. Therefore, when the laser power is low, input energy cannot break the oxide film, which hinders the interaction between each layer of metal. This will leads to defects such as pores and cracks during aluminum alloy processing. In order to obtain high-strength aluminum alloy in SLM, it is necessary to prevent it from oxidizing. Aluminum alloy has high thermal conductivity and laser reflectivity, and the energy utilization rate is lower than other metals [19, 20]. SLM processed high-silicon aluminum alloy materials can significantly refine its microstructure and improve their performance. E.O. Olakanmi proved [21, 22] that the density of Al–12Si depends on the intensity of the laser and the scanning speed, and the direction of the voids and the density of the processed alloy vary greatly on process parameters. Prashanth [20, 23, 24] studied the influence of the microstructure of selective laser melting fabricated Al–12Si alloy on the mechanical properties. Those experiments employed two different ways of scanning speeds and other parameters unchanged, and results shown that the higher heat treatment temperature is, the coarser the grains of the sample becomes. Also the tensile strength decreases and the fracture toughness increases with higher heat treatment temperature. Therefore, the size and shape of grains in microstructure have serious impact on the mechanical properties of the alloys, and alloys show different mechanical properties with different process parameters. But different process parameters will introduce process defects during selective laser melting.

Al–42Si alloy prepared by SLM has defects such as pores, uneven microstructure and residual stress, which will significantly reduce the

Table 1. List of the process parameters selected to fabricate Al–42Si samples. The energy density is calculated by Eq. (1).

Samples	Laser power (W)	Scanning speed (mm/s)	Layer thickness (μm)	Hatch spacing (mm)	Energy density (J/mm^3)
1#	320	1455	50	0.11	40.0
2#	320	1455	50	0.13	33.8
3#	320	1355	50	0.11	42.9
4#	340	1455	50	0.11	42.5

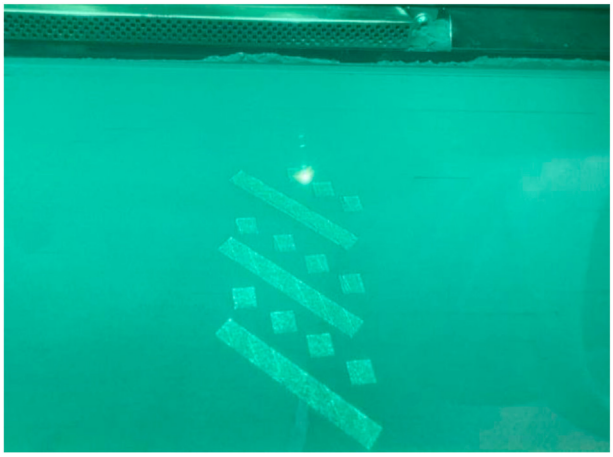

Figure 3. Selective laser melting process of high-silicon Al–42Si alloy samples.

elongation and fatigue resistance of the alloy. In order to improve the mechanical properties of Al–42Si alloy, researchers have developed a variety of post-treatment methods, such as heat treatment, hot isostatic pressing, and friction stir processing [25, 26, 27, 28]. In this paper, selective laser melting technology is used to prepare Al–42Si alloy. The printability of Al–42Si alloy has been verified by experiments, and we also have studied the formation of defects in Al–42Si alloy microstructure and process under different process parameters, optimized the additive manufacturing process parameters. In addition, this paper studies the microstructure and mechanical properties of the Al–42Si alloy material during the heat treatment process to improve its comprehensive performance.

2. Experimental materials and methods

2.1. Material analysis

In this paper, Al–42Si alloy powder was selected as the material, which was prepared by gas atomization technology with particle size

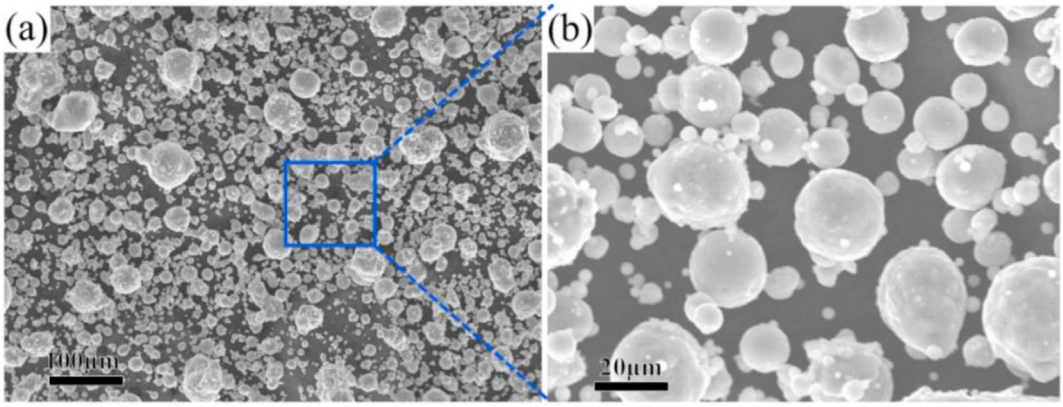

Figure 2. Scanning electron microscope morphologies of Al–42Si powder particles.

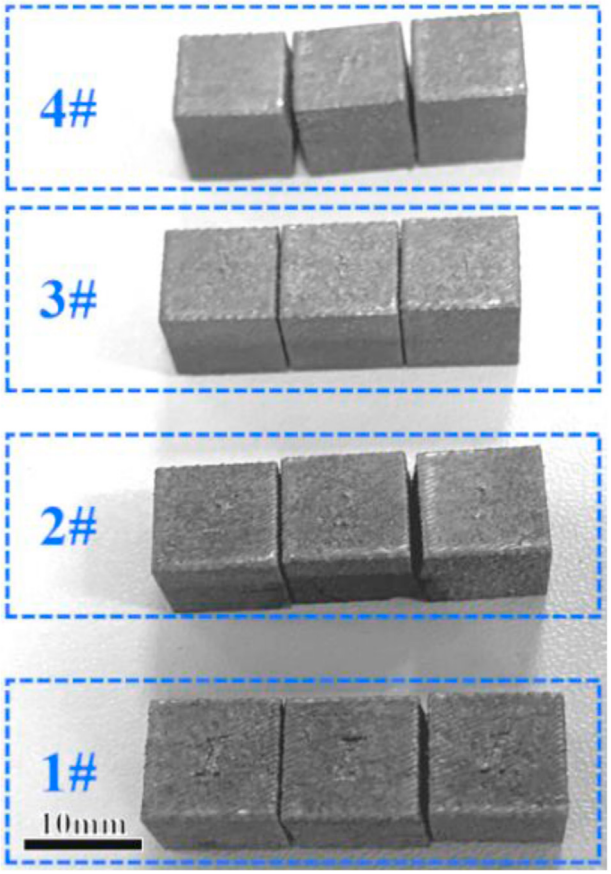

Figure 4. Selective laser melting fabricated Al–42Si alloy samples.

ranging from 20μm to 60μm. The particle size was analyzed by laser diffraction particle size analyzer (Mastersizer 3000E), and the particle size distribution as shown in Figure 1. The particle refractive index is 1.268 and the particle absorption rate is 1.000. The typical values of D_{10}, D_{50} and D_{90} were 11.1μm, 41.8μm and 87.0μm, respectively. The medium particle size of the powder is 41.8μm, and the thickness of the printing layer is 50μm, which meets the printing conditions.

The morphologies of powder was observed using Coxem EM-30 Plus scanning electron microscope, as shown in Figure 2. The powder morphology of Al–42Si alloy in Figure 2 was obtained. The particle size of the powder is about 20–60μm, and there are some smaller particles. These small particles adhere to the large particles to form satellite spheres, Also some special-shaped powders that possess the weird shapes in the powder. The satellites ball and special-shaped powder are irregular particles, which make the fluidity and dispersion of powder worse. Those irregular particles are disadvantageous in powder laying process of selective laser melting [29, 30].

2.2. Selective laser melting process

The samples of Al–42Si alloy were fabricated using a EOSINT M280 equipment. The equipment is equipped with IPG ytterbium laser (a maximum power of 400W and a spot diameter of 70 μm), which can provide high performance, high stability, and high quality laser for printing process. The fabrication of the samples was carried out in an argon atmosphere with less than 0.05% oxygen. The building platform was preheated at 80 °C. a stripe scanning strategy was employed during SLM process. Bulk samples with dimensions of 10 × 10 × 10 mm^3 were built for microstructural analysis and hear treatments, respectively. Four groups of SLM-fabricated samples were obtained according to Table 1 parameters. Based on sample 1#, and change the scanning spacing, scanning speed and laser power to obtain parameter 2#, parameter 3# and parameter 4#.

The relationship between energy density and other parameters is as follows [31]:

$$E = \frac{P}{h.V.D} \tag{1}$$

Where E is energy density (J/mm^3), P is laser power (W), D is the hatch spacing (mm), V is the scanning speed (mm/s), h is the layer thickness (mm). The SLM-fabricated process is shown in Figure 3.

After finishing printing, wait for the temperature of samples drop to room temperature, then take out the samples and the substrate together, and then use wire cutting to take down the samples from the substrate.

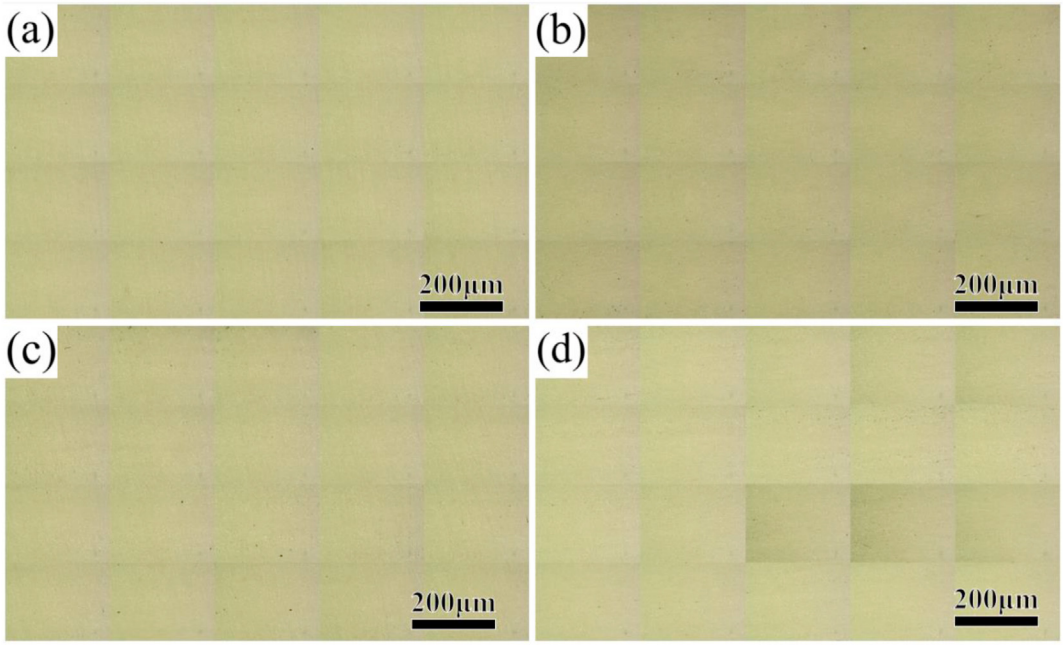

Figure 5. Optical micrographs for the cross-section of SLM-fabricated samples using different process parameters according to Table 1.

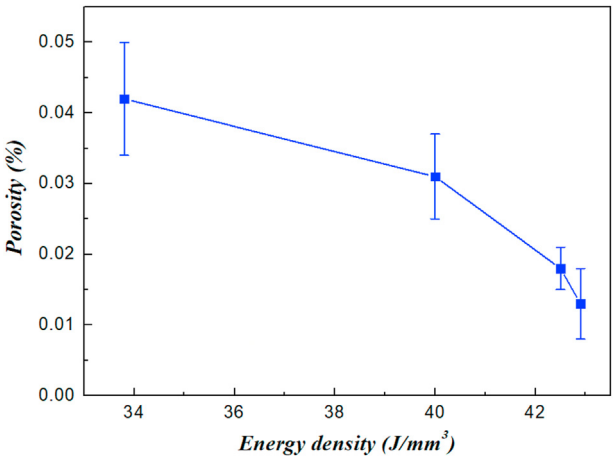

Figure 6. Variation in relative porosity with energy density for SLM fabricated Al–42Si samples with different process parameters.

Finally, four groups of cube samples with side length of 10mm were obtained, the samples fabricated by SLM were shown in Figure 4.

2.3. Characterization methods

The cross sections of SLM-fabricated samples parallel to building direction were ground and polished according to standard metallographic procedures, and the microstructure was observed by Olympus optical microscope (OM) and Coxem EM-30 Plus scanning electron microscope (SEM) equipped with an energy dispersive spectrometer (EDS). Metallographic preparation was carried out for each set of parameter samples, and the grinding surface was selected as the side surface (longitudinal section) for observation. Relative density calculation was done with an optical microscope pictures taken from the middle part of the longitudinal direction in each sample using Image J software. In each sample, at least 20 micrographs were assessed for relative density measurements.

The heat treatment were conducted to reduce the stress and make microstructure homogeneous compared to SLM-fabricated samples. The heat treatment temperature and time were set at 550 °C for 24 h. The heat treatment was conducted in a muffle furnace and the samples were retrieved from furnace and cooled in air. The microhardness measurements were conducted with a standardized Vickers measuring test device (HVS–1000B) at a load of 4.908N (500g) and a dwell time of 10(s) on the surface of longitudinal section of SLM-fabricated and heat treatment samples with polished surfaces. The every values of microhardness were average of 10 times measurements.

3. Results and discussion

3.1. The relative density of SLM fabricated Al–42Si alloy samples

Figure 5 displays the OM images of SLM fabricated Al–42Si samples with different process parameters. The images were observed with an optical microscope, and 20 pictures were taken in sequence by selecting different areas. It is observed from the images that the printability of Al–42Si alloy samples is good, and there is no obvious crack in SLM fabricated samples. Also some large silicon phase can be observed in the images, and the black spots can be seen on the surface, which are considered as porosity. The relative porosity of the four groups of samples were respectively 0.031%, 0.042%, 0.013% and 0.018% by defects calculation with software. According to the data, the relationship between energy density and porosity is characterized, as shown in Figure 6.

Figure 6 shows the variation in relative porosity with energy density for SLM fabricated Al–42Si samples, which can be seen that the relative porosity of the samples increases with the increase of the input energy density. The density of the alloy is negatively correlated with porosity. The porosity mainly contain non-fusion and pores in selective laser melting process. When the energy density is 42.9J/mm^3, the relative porosity is the lowest (0.013%) and the relative density is the highest. When the energy density is 35.8J/mm^3, the relative porosity reaches the lowest of 0.042% and the relative density is the lowest. Compared with 3#, 1# reduces the scanning speed of 3#; Compared with 4#, the laser power of 1# increases and the density of the alloy increases.

The melting ability of the powder decreases with the input energy density being low. If scanning speed is fast at this time, the cooling rate of the molten pool will be accelerated. At this time, the bubbles released during the melting of the powder cannot be discharged, and pores will appear during SLM process. When input energy density reach the highest, the excessive energy will pass through the metal powder to melt the

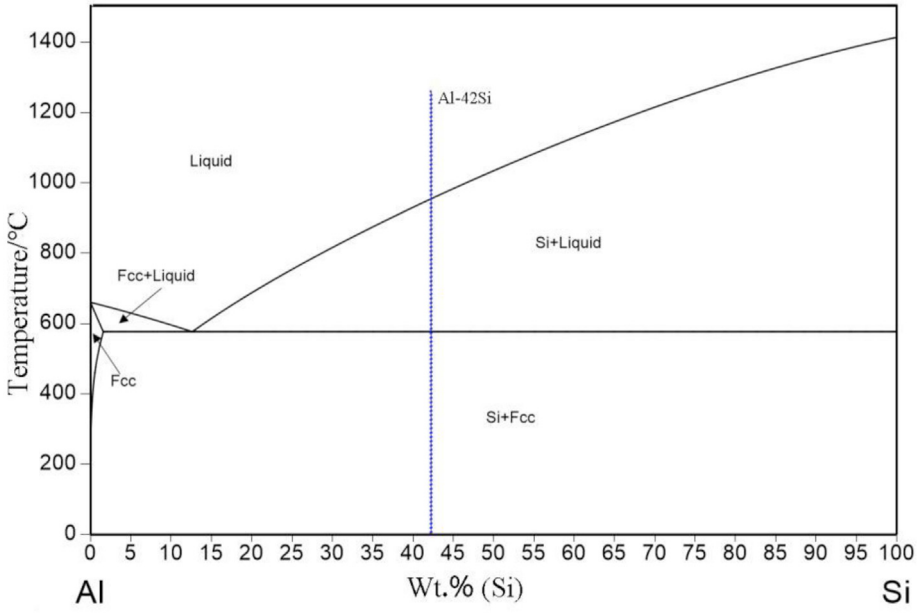

Figure 7. Phase diagram of binary Al–Si alloy [34].

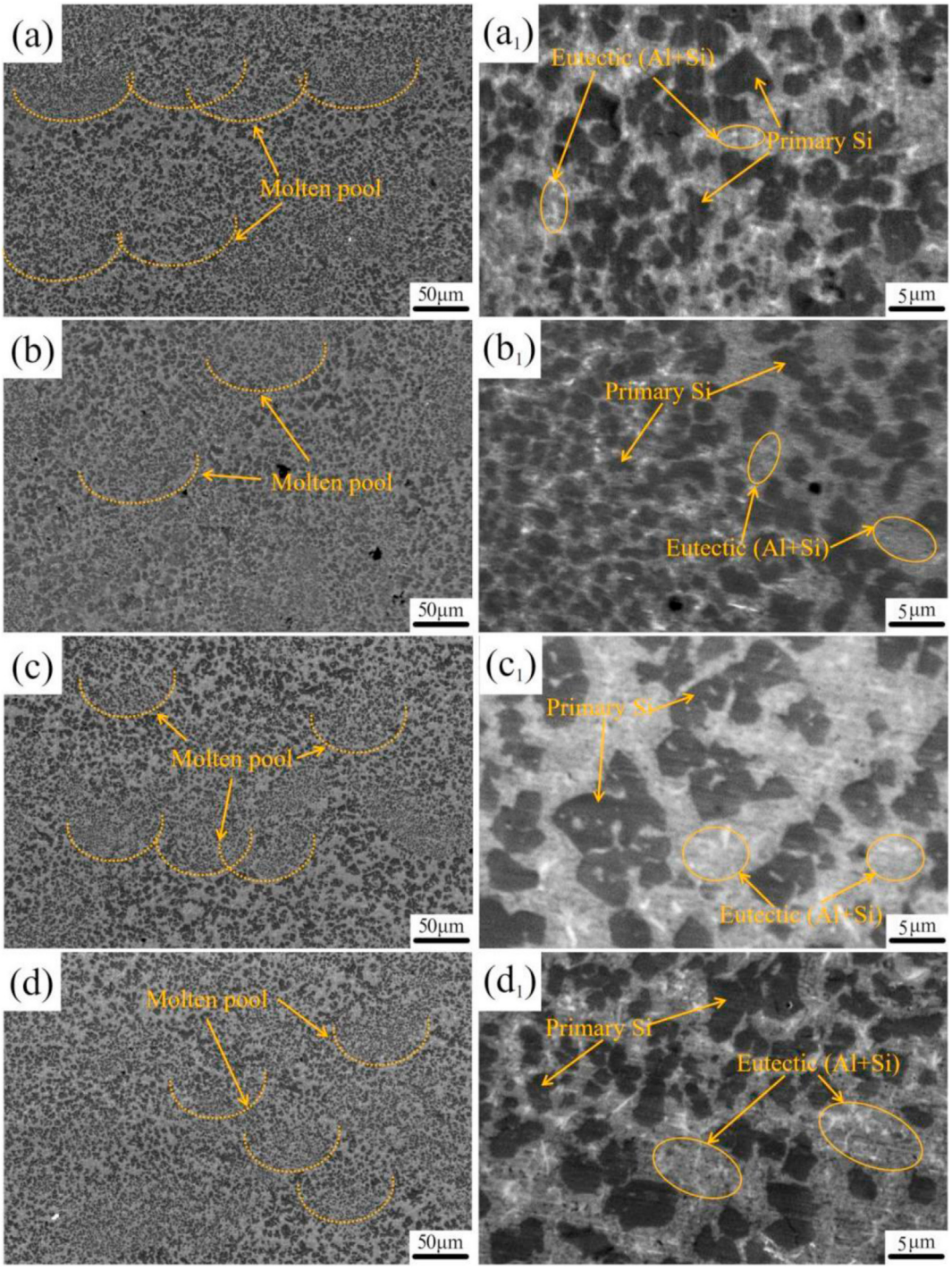

Figure 8. SEM-SE micrographs of the cross section of SLM fabricated Al–42Si alloy at different process parameters.

solidified metal again, increasing the thermal stress between metals and cracks being prone to appear [32, 33]. Moreover, decreasing the scanning speed and appropriately increasing the laser power can increase the density of the alloy, and the influence is greater than the energy density.

3.2. Microstructure characterization of SLM fabricated Al–42Si alloy

Figure 7 shows the phase diagram of a binary Al–Si alloy. High-silicon content alloys fall in the range of hypereutectic Al–Si alloys, and there are two phases at room temperature, named primary β-Si and (α+β) eutectic phase upon equilibrium solidification. The microstructure of hypereutectic alloy is composed of β(Si)+eutectic (α+β). In this study, the silicon content is 42%, is a hypereutectic alloy, its equilibrium microstructure composition of eutectic structure (α+β) and primary silicon β(Si).

Figure 8 shows microstructures of SLM-fabricated Al–42Si alloys at different process parameters. As can be seen from Figure 8, although this alloy has a high silicon content, many primary silicon phases are formed in microstructures, it can still see the morphology of the molten pool clearly, as shown by orange arrow in figures. The typical microstructures of SLM-fabricated Al–42Si alloy mainly present primary silicon phases (β-Si) and (α+β) eutectic phases, which is similar to phase composition in as-cast alloy. Also some white oxide particles can be seen in microstructure, these white oxide particles are mainly oxides containing Al and Si, which may be formed by the oxygen contained in the additive

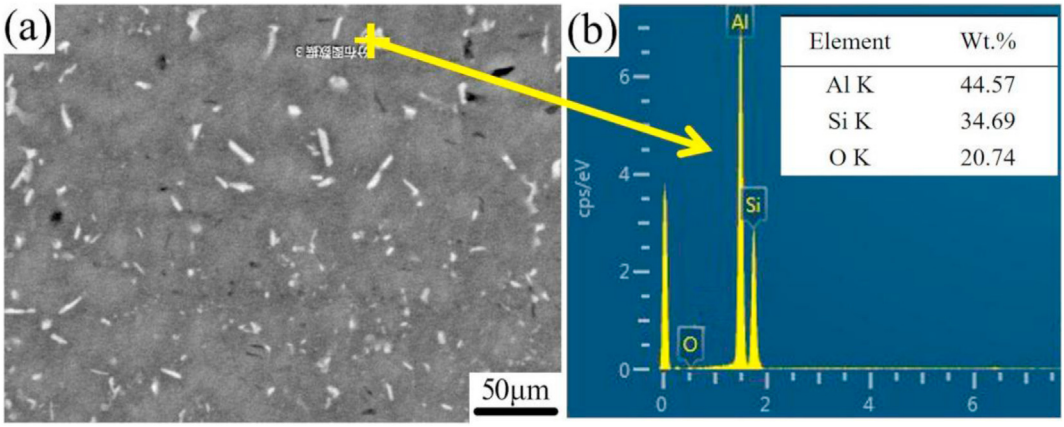

Figure 9. SEM-SE micrograph and composition distribution of white oxide particles in SLM-fabricated Al–42Si alloy using EDS.

manufacturing metal powder and the oxygen in the atmosphere being sucked into the alloy during SLM process, as shown in Figure 9.

The molten pools shown different length and width under different process parameters. When compared with the size of the primary silicon phases in the microstructures of SLM-fabricated Al–42Si alloys, the sizes of primary silicon phases in the center of the molten pool is obviously smaller than that at boundary of molten pool. After measuring the size of the molten pool from images in Figure 8, take its average value. The pool sizes of four groups samples are 130 ± 12μm for 1#, 140 ± 10μm for 2#, 125 ± 10μm for 3#, and 126 ± 8μm for 4#, respectively (in order of parameters). According to the size of the molten pool, when the energy density is the highest (3#, 42.9J/mm^3), the molten pool is the smallest, which is 125 ± 10μm. When the energy density is the smallest (2#, 35.8J/mm^3), the molten pool is the largest, which is 140 ± 10μm.

Figure 10 shows SEM-SE morphologies and composition distribution of SLM-fabricated Al–42Si alloy. Figure 10(a) reflects the microstructures at the boundary of molten pool of SLM-fabricated Al–42Si alloy. The Si content in the black part of Figure 10(a) is 77.22%, which indicates that is primary silicon phases with high Si contents. In EDS results of the gray part, the highest peak is Al, and its content value is 72.45%, which indicates that it is eutectic structure. Figure 10(b) shows the area occupied by Al and Si, in which the proportion of Al is 57.5% and that of Si is 41.1%, which is consistent with the nominal materials composition.

The size of primary silicon phases was measured according to the longitudinal section images of the samples. It can be seen that when the energy density is the largest (3#, 42.9J/mm^3), the maximum value of the primary silicon phase is also the largest, and the silicon phase size ranges from 3.3 to 9.4μm. With the decrease of the energy density, the

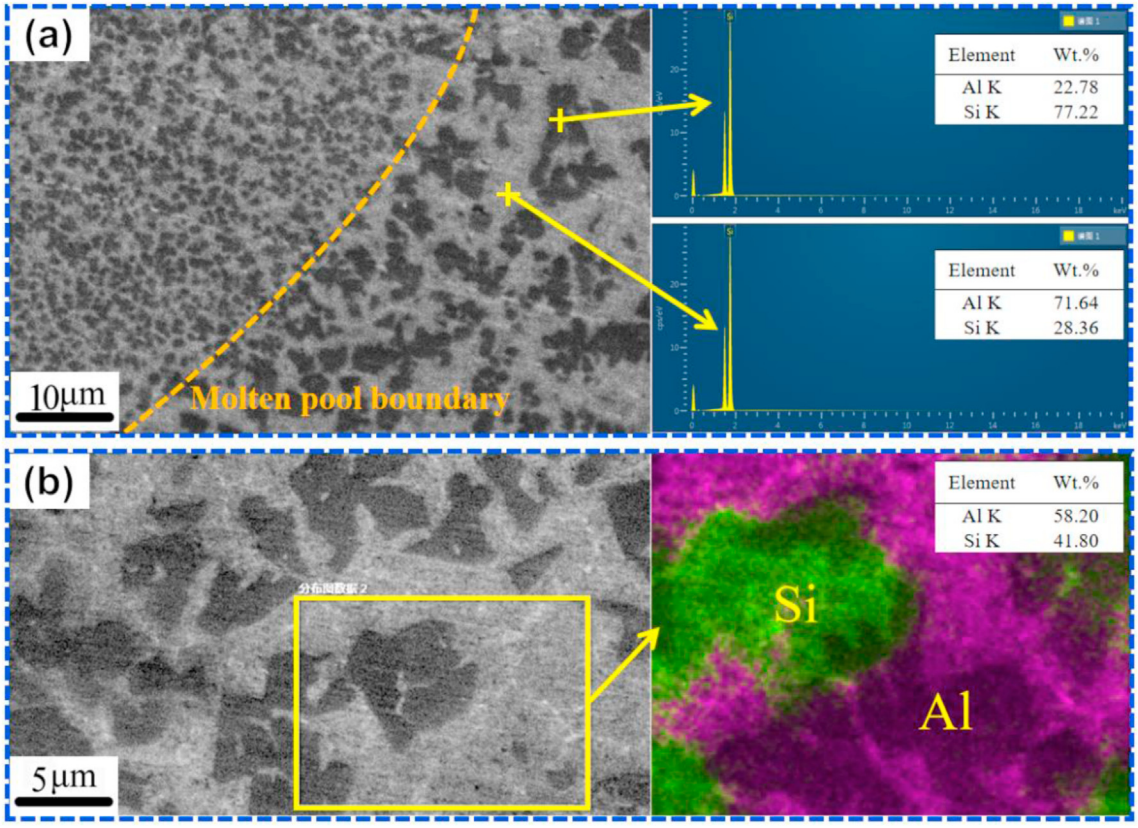

Figure 10. Morphologies and composition distribution of SLM-fabricated Al–42Si alloy using SEM-SE with EDS.

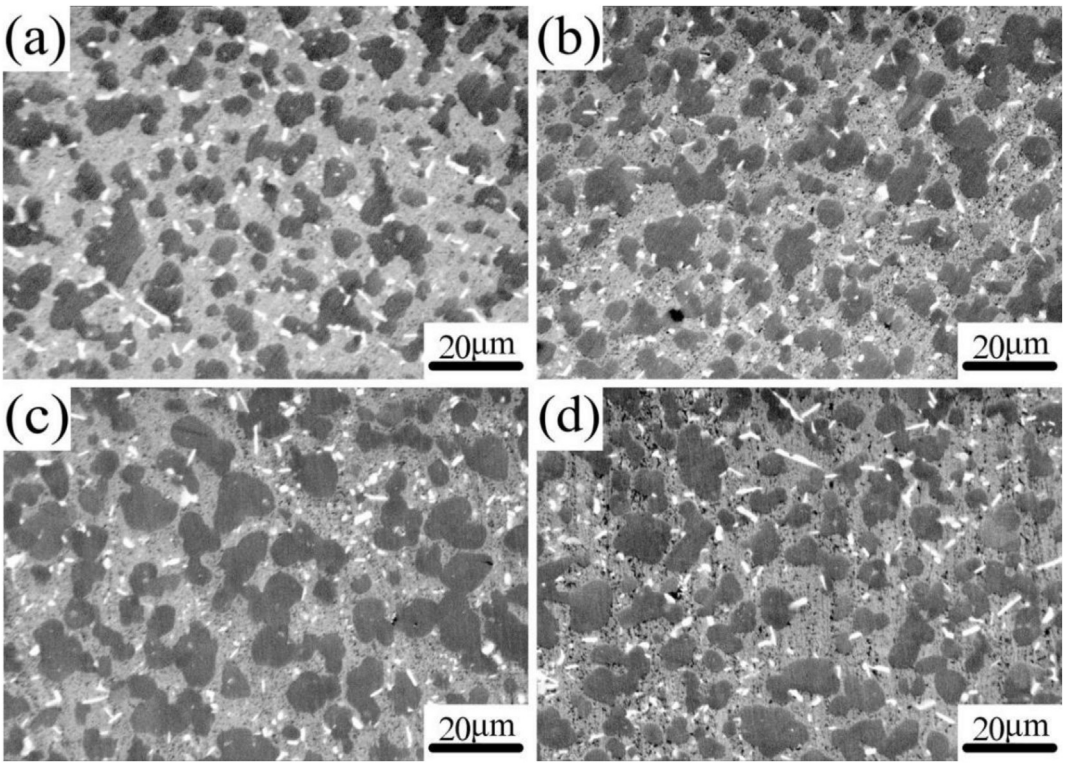

Figure 11. SEM-SE micrographs of SLM-fabricated Al–42Si alloy after heat treatment, (a) 1#, (b) 2#, (c) 3#, (d) 4#.

maximum value of the primary silicon phase also decreases gradually. When the energy density is the lowest (2#, 35.8J/mm^3), the maximum value of the primary silicon phase is the minimum, and the size range of primary silicon is about 2.9–6.5μm. The size range of primary silicon of the two groups of energy density is 3.2–7.5μm for sample 1# and 3.3–7.6μm for sample 4#, that is, the order of primary silicon size is 3# > 4#>1# > 2# (according to the maximum value). Therefore, the higher the input energy density, the smaller the density of the primary silicon. This is because the energy density is higher, the more heat is released with the powder melted during selective laser melting process, the more

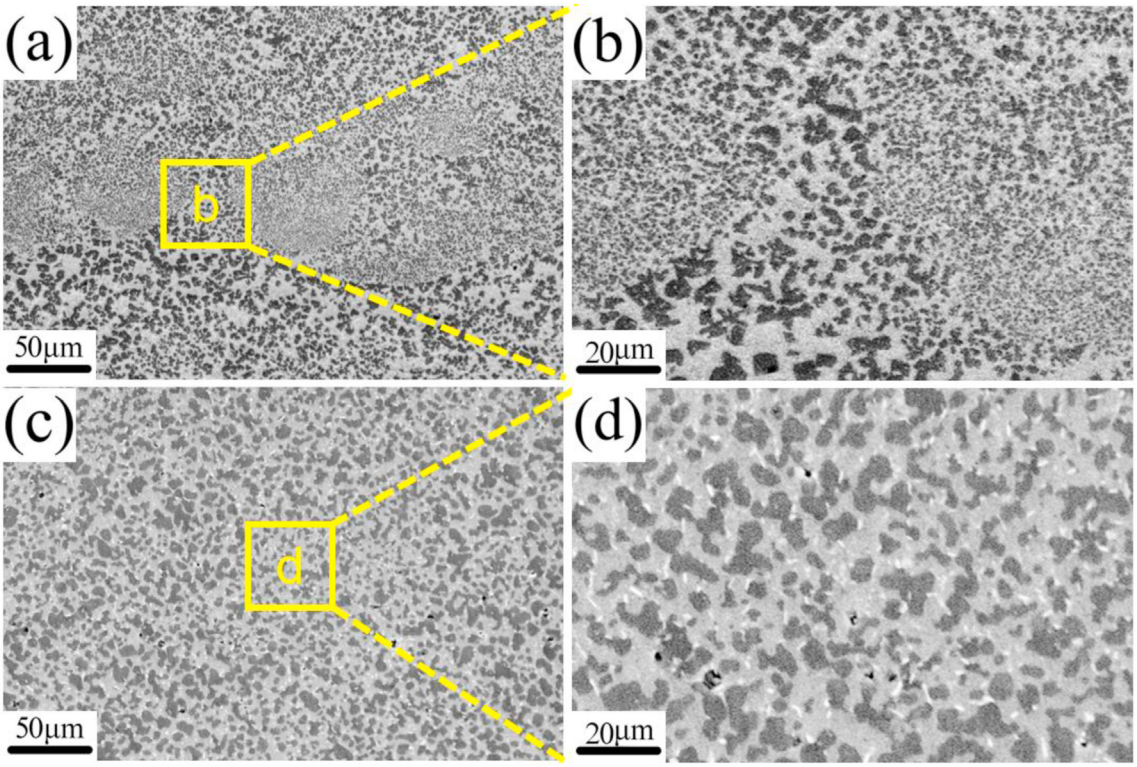

Figure 12. SEM-SE micrographs and distribution of primary Si phases of 3# Al–42Si alloy at SLM-fabricated state (a) (b), and heat treatment state (c) (d).

Table 2. Hardness values (*HV*).

	1	2	3	4
SLMed	156.3	178.7	179.9	169.6
Heat treatment	120.9	108.4	101.5	115.1

temperature rises, so the silicon phase grows. However, because the rapid cooling hinders the diffusion of silicon atoms, so the growth of silicon is limited to some extent, when compared with as-cast alloys.

3.3. Microstructures of SLM fabricated Al–42Si alloy after heat treatment

After heat treatment, the samples were grinded into metallography, and their microstructures were observed by SEM-SE, as shown in Figure 11. Some little primary silicon phases are merged, and the morphologies of primary silicon phase changed from a sharp corner to a round shape in some extent in microstructure of SLM-fabricated Al–42Si alloy after heat treatment. Heat treatment process can eliminate or reduce the residual stress, make the microstructures become more stable, and the composition distribution is also homogeneous [35, 36]. Also white oxides containing Al and Si are increased after heat treatment, and the size of these particles are grew.

Since the heat treatment temperature is close to the eutectic temperature, the size of primary silicon grows gradually during heat-treated process. By measuring the size of primary silicon, the size of silicon can be obtained:1# increases to 8.3μm, 2# increases to 7.3μm, 3# increases to 9.4μm, and 4# increases to 8.9μm (because the microstructure is uniform after heat treatment, the silicon phase size is averaged). The four groups of samples were compared, and the size order was 3# > 4#>1# > 2#. This size order remained unchanged with that before heat treatment, and was one-to-one corresponding to the input energy density, that is, the greater the input energy density, the greater the primary silicon.

Figure 12 shows the morphologies and distribution of primary Si phases of SLM-fabricated state and heat treatment state of sample 3#. The distribution of primary silicon phase in SLM-fabricated state is not uniform and the size is not consistent, which can clearly see the arc of the molten pool boundary. The size of primary silicon phase in the center of the molten pool is smaller than that at the boundary obviously. Heat treatment can effectively eliminate the internal defects of the samples and improve the primary silicon phases distribution in SLM-fabricated Al–42Si alloy. Therefore, the sample microstructure after heat treatment is more uniform, the size and morphology of primary silicon are consistent, and the boundary and morphology of molten pool are more difficult to distinguish.

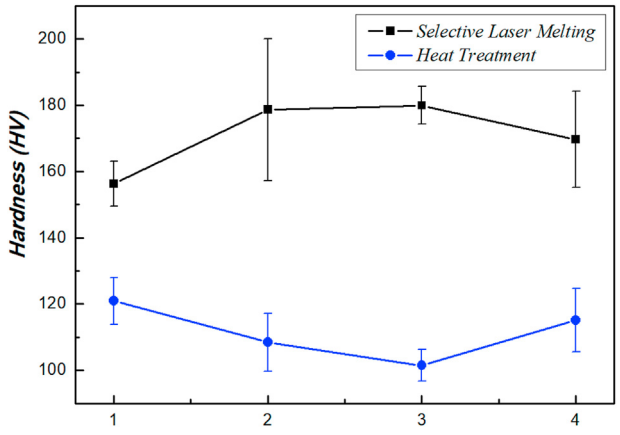

Figure 13. Hardness value before and after heat treatment.

3.4. The hardness of SLM-fabricated Al–42Si alloy

The measured hardness values of the SLM-fabricated and heat-treated samples are averaged respectively, and the obtained hardness values are shown in Table 2. According to hardness values obtained in Table 2, a line graph is made as shown in Figure 13. The results show that the hardness of the alloy increases with the energy density from 40.0J/mm^3 to 42.9J/mm^3, which is consistent with the change of density with the energy density. When the porosity in the alloy is high, the hardness load will cause the material to collapse, leading to the decrease of hardness.

However, when the energy density is 35.8J/mm^3, the hardness of the alloy is obviously higher, because the selective laser melting is a process of rapid heating and cooling, and has the effect of fine grain strengthening and the size of primary Si particles. According to the Orowan reinforcement equation [37, 38]:

$$\nabla\sigma = \frac{0.4MG_m \ln\left(\frac{\sqrt{2/3}d_p}{b}\right)}{2\pi\lambda(1-\nu)^{1/2}} \tag{2}$$

Where d_p is the average particle size; M is the average orientation factor; b is the bergheit vector of alloy; G_m is the shear modulus of alloy; ν is Poisson's ratio; λ is the particle spacing. Therefore, the larger the Si particle size, the higher the strength. According to the silicon phase size measured in 3.1, the size of 3# is the largest, so the strength of 3# sample is highest. It can be calculated from Eq. (2) that the contribution of primary Si phase to the hardness of 3# sample increases by 15.7HV compared with 1# sample. The calculated result is close to the experimental increment of 23.6HV in 1# and 3# samples. It also can be seen from the change of hardness in SLM-fabricated alloy and heat treatment alloy, the change of 1# selective laser melting technology decreases, but its hardness increases obviously. After heat treatment, the internal residual stress is eliminated and the alloy possesses distribution uniformity and the hardness of the alloy decrease with different degrees. Sample 3# has the highest hardness with SLM-fabricated state, and decreases most after heat treatment, and its hardness value is the lowest among the four groups after heat treatment. The hardness of sample 1# with the lowest value in SLM-fabricated state, and with least decreases after heat treatment.

4. Conclusion

In this study, the successful process of SLM-fabricated Al–42Si alloy will expand the application range of Al–42Si alloy especially in aerospace, electronics and semiconductors. Many parts with complex shapes can be made by SLM technology, but the manufacturing of these parts is still limited by their forming methods. Therefore, Al–42Si alloy successfully prepared by SLM technology will further promote its application scope and field.

(1) The relative density of SLM-fabricated Al–42Si alloy is positively correlated with the laser energy density during selective laser melting process. The relative density of the alloy is also affected by scanning speed, laser power and scanning spacing. And the relative density of the alloy increases first and then decreases with the increase of the laser energy density.

(2) The higher the input laser energy density, the larger the primary silicon size in SLM-fabricated Al–42Si alloy and the smaller size of the molten pool, and the growth of primary silicon will be limited, due to rapid cooling. n summary, the optimal process parameters are laser power is 320W, the scan rate is 1355 mm/s, the layer thickness is 50μm, and the scan pitch is 0.11mm in this study.

(3) The hardness of SLM-fabricated Al–42Si alloy increases as the energy density increases in the range of 40.0J/mm^3 to 42.9J/mm^3, and the hardness of SLM-fabricated Al–42Si alloy decreases

with the relative density decreases. the hardness decreases after heat treatment.

(4) After heat treatment, the size of the primary silicon phase of SLM-fabricated Al–42Si alloy increases, and the distribution of the microstructure is uniform. Heat treatment process can eliminate residual stress and improve internal defects, and the distribution of primary silicon phase in microstructures changes from inhomogeneous homogeneous. Also, the size of the primary silicon phase is increased about 1~2μm after heat treatment.

Declarations

Author contribution statement

Xiaoye Cai, Tong Liu: Conceived and designed the experiments; Performed the experiments; Analyzed and interpreted the data; Wrote the paper.

Xuan Yan, Zonghui Cheng and Lu Pan: Conceived and designed the experiments; Contributed reagents, materials, analysis tools or data.

Zongjun Tian, Liangshun Luo: Analyzed and interpreted the data; Contributed reagents, materials, analysis tools or data.

Yanqing Su: Conceived and designed the experiments; Analyzed and interpreted the data; Wrote the paper.

Funding statement

Mr. Tong Liu was supported by National Natural Science Foundation of China [52001001], Scientific Research Foundation of AnHui Polytechnic University [2020YQQ005], and Industrial Collaborative Innovation Foundation of AnHui Polytechnic University-Fanchang District [2021FCCYXTA2].

Data availability statement

Data included in article/supp. material/referenced in article.

Declaration of interest statement

The authors declare no conflict of interest.

Additional information

No additional information is available for this paper.

References

[1] Z. Cai, C. Zhang, R. Wang, C. Peng, X. Wu, H. Li, Microstructure, mechanical and thermo-physical properties of Al–50Si–xMg alloys, Mater. Sci. Eng., A 730 (2018) 57.

[2] Y.D. Jia, P. Ma, K.G. Prashanth, G. Wang, J. Yi, S. Scudino, F.Y. Cao, J.F. Sun, J. Eckert, Microstructure and thermal expansion behavior of Al-50Si synthesized by selective laser melting, J. Alloys Compd. 699 (2017) 548.

[3] N. Kang, P. Coddet, M. Ammar, H. Liao, C. Coddet, Characterization of the microstructure of a selective laser melting processed Al-50Si alloy: effect of heat treatments, Mater. Char. 130 (2017) 243.

[4] A.W. Shah, S. Ha, B. Kim, Y. Yoon, H. Lim, S.K. Kim, Effect of Al2Ca addition and heat treatment on the microstructure modification and tensile properties of hypo-eutectic Al–Mg–Si alloys, Materials 14 (2021) 4588.

[5] Y.M. Wang, T. Voisin, J.T. McKeown, J. Ye, N.P. Calta, Z. Li, Z. Zeng, Y. Zhang, W. Chen, T.T. Roehling, R.T. Ott, M.K. Santala, P.J. Depond, M.J. Matthews, A.V. Hamza, T. Zhu, Additively manufactured hierarchical stainless steels with high strength and ductility, Nat. Mater. 17 (2018) 63.

[6] J.H. Martin, B.D. Yahata, J.M. Hundley, J.A. Mayer, T.A. Schaedler, T.M. Pollock, 3D printing of high-strength aluminium alloys, Nature 549 (2017) 365.

[7] T. Maeshima, K. Oh-ishi, Solute clustering and supersaturated solid solution of AlSi10Mg alloy fabricated by selective laser melting, Heliyon 5 (2019) e1186.

[8] M. Velasco-Castro, E. Hernández-Nava, I.A. Figueroa, I. Todd, R. Goodall, The effect of oxygen pickup during selective laser melting on the microstructure and mechanical properties of Ti–6Al–4V lattices, Heliyon 5 (2019), e2813.

[9] T. Allam, K.G. Pradeep, P. Köhnen, A. Marshal, J.H. Schleifenbaum, C. Haase, Tailoring the nanostructure of laser powder bed fusion additively manufactured maraging steel, Addit. Manuf. 36 (2020), 101561.

[10] S. Shamsdini, S. Shakerin, A. Hadadzadeh, B.S. Amirkhiz, M. Mohammadi, A trade-off between powder layer thickness and mechanical properties in additively manufactured maraging steels, Mater. Sci. Eng., A 776 (2020), 139041.

[11] C. Qiu, N.J.E. Adkins, M.M. Attallah, Selective laser melting of Invar 36: microstructure and properties, Acta Mater. 103 (2016) 382.

[12] G. Liu, J. Xiong, L. Tang, Microstructure and mechanical properties of 2219 aluminum alloy fabricated by double-electrode gas metal arc additive manufacturing, Addit. Manuf. 35 (2020), 101375.

[13] W. Lefebvre, G. Rose, P. Delroisse, E. Baustert, F. Cuvilly, A. Simar, Nanoscale periodic gradients generated by laser powder bed fusion of an AlSi10Mg alloy, Mater. Des. 197 (2021), 109264.

[14] S. Goel, M. Neikter, J. Capek, E. Polatidis, M.H. Colliander, S. Joshi, R. Pederson, Residual stress determination by neutron diffraction in powder bed fusion-built Alloy 718: influence of process parameters and post-treatment, Mater. Des. 195 (2020), 109045.

[15] W. Tillmann, C. Schaak, J. Nellesen, M. Schaper, M.E. Aydinöz, K.P. Hoyer, Hot isostatic pressing of IN718 components manufactured by selective laser melting, Addit. Manuf. 13 (2017) 93.

[16] P. Qi, B. Li, T. Wang, L. Zhou, Z. Nie, Evolution of microstructural homogeneity in novel Ti-6Zr-5Fe alloy fabricated by selective laser melting, Mater. Char. 171 (2021), 110729.

[17] R. Alaghmandfard, D. Chalasani, A. Hadadzadeh, B.S. Amirkhiz, A. Odeshi, M. Mohammadi, Dynamic compressive response of electron beam melted Ti–6Al–4V under elevated strain rates: microstructure and constitutive models, Addit. Manuf. 35 (2020), 101347.

[18] T. Peng, Y. Zhu, M. Leu, D. Bourell, Additive manufacturing-enabled design, manufacturing, and lifecycle performance, Addit. Manuf. 36 (2020), 101646.

[19] M.L. Montero-Sistiaga, R. Mertens, B. Vrancken, X. Wang, B. Van Hooreweder, J. Kruth, J. Van Humbeeck, Changing the alloy composition of Al7075 for better processability by selective laser melting, J. Mater. Process. Technol. 238 (2016) 437.

[20] R. Baitimerov, P. Lykov, D. Zherebtsov, L. Radionova, A. Shultc, K. Prashanth, Influence of powder characteristics on processability of AlSi12 alloy fabricated by selective laser melting, Materials 11 (2018) 742.

[21] E.O. Olakanmi, R.F. Cochrane, K.W. Dalgarno, Densification mechanism and microstructural evolution in selective laser sintering of Al–12Si powders, J. Mater. Process. Technol. 211 (2011) 113.

[22] E.O. Olakanmi, R.F. Cochrane, K.W. Dalgarno, A review on selective laser sintering/melting (SLS/SLM) of aluminium alloy powders: processing, microstructure, and properties, Prog. Mater. Sci. 74 (2015) 401.

[23] K.G. Prashanth, S. Scudino, J. Eckert, Defining the tensile properties of Al-12Si parts produced by selective laser melting, Acta Mater. 126 (2017) 25.

[24] J. Suryawanshi, K.G. Prashanth, S. Scudino, J. Eckert, O. Prakash, U. Ramamurty, Simultaneous enhancements of strength and toughness in an Al-12Si alloy synthesized using selective laser melting, Acta Mater. 115 (2016) 285.

[25] Y.D. Jia, L.B. Zhang, P. Ma, S. Scudino, G. Wang, Thermal expansion behavior of Al – xSi alloys fabricated using selective laser melting, Prog. Addit. Manufact. 5 (2020) 247.

[26] N. Kang, P. Coddet, H. Liao, C. Coddet, Macrosegregation mechanism of primary silicon phase in selective laser melting hypereutectic Al – high Si alloy, J. Alloys Compd. 662 (2016) 259.

[27] L. Xi, S. Guo, K. Ding, K.G. Prashanth, B. Sarac, J. Eckert, Effect of nanoparticles on morphology and size of primary silicon and property of selective laser melted Al-high Si content alloys, Vacuum 191 (2021), 110405.

[28] Y. Xu, Y. Deng, D. Casari, R.H. Mathiesen, Y. Li, In-situ X-radiographic study of nucleation and growth behaviour of primary silicon particles during solidification of a hypereutectic Al-Si alloy, J. Alloys Compd. 832 (2020), 154948.

[29] M. Wei, S. Chen, J. Liang, C. Liu, Effect of atomization pressure on the breakup of TA15 titanium alloy powder prepared by EIGA method for laser 3D printing, Vacuum 143 (2017) 185.

[30] C. Zhong, J. Chen, S. Linnenbrink, A. Gasser, S. Sui, R. Poprawe, A comparative study of inconel 718 formed by high deposition rate laser metal deposition with GA powder and PREP powder, Mater. Des. 107 (2016) 386.

[31] Y. Wang, L. Luo, T. Liu, B. Wang, L. Luo, J. Zhao, L. Wang, Y. Su, J. Guo, H. Fu, Tuning process parameters to optimize microstructure and mechanical properties of novel maraging steel fabricated by selective laser melting, Mater. Sci. Eng., A 823 (2021), 141740.

[32] D. Bayoumy, D. Schliephake, S. Dietrich, X.H. Wu, Y.M. Zhu, A.J. Huang, Intensive processing optimization for achieving strong and ductile Al-Mn-Mg-Sc-Zr alloy produced by selective laser melting, Mater. Des. 198 (2021), 109317.

[33] Z. Hu, X. Nie, Y. Qi, H. Zhang, H. Zhu, Cracking criterion for high strength Al–Cu alloys fabricated by selective laser melting, Addit. Manuf. 37 (2021), 101709.

[34] G.V. Voort, J. Asensio-Lozano, The Al-Si phase diagram, Microsc. Microanal. 15 (2009) 60.

[35] P. Wang, C. Gammer, F. Brenne, K.G. Prashanth, Microstructure and mechanical properties of a heat-treatable Al-3.5Cu-1.5Mg-1Si alloy produced by selective laser melting, Mater. Sci. Eng., A (2018) 562.

[36] W. Tu, J. Tang, L. Ye, L. Cao, Y. Zeng, Q. Zhu, Y. Zhang, S. Liu, L. Ma, J. Lu, B. Yang, Effect of the natural aging time on the age-hardening response and precipitation behavior of the Al-0.4Mg-1.0Si-(Sn) alloy, Mater. Des. 198 (2021), 109307.

[37] R. Shu, X. Jiang, H. Sun, Z. Shao, T. Song, Z. Luo, Recent researches of the bio-inspired nano-carbon reinforced metal matrix composites, Compos. Appl. Sci. Manuf. 131 (2020), 105816.

[38] J. Zhang, T. Jia, H. Zhu, Z. Xie, Microstructure and mechanical properties of in-situ TiC reinforced FeCoNiCu2.0 high entropy alloy matrix composites, Mater. Sci. Eng., A 822 (2021), 141671.